Robust Vehicular Localization and Map-Matching in Urban Environments with IMU, GNSS, and Cellular Signals

Zaher M. Kassas, *Senior Member, IEEE,* Mahdi Maaref, Joshua Morales, *Student Member, IEEE,* Joe Khalife, *Student Member, IEEE,* and Kimia Shamaei, *Student Member, IEEE,*

***Abstract*—A framework for ground vehicle localization that uses cellular signals of opportunity (SOPs), a digital map, an inertial measurement unit (IMU), and a global navigation satellite system (GNSS) receiver is developed. This framework aims to enable localization in urban environment where GNSS signals could be unusable or unreliable. The proposed framework employs an extended Kalman filter (EKF) to fuse pseudorange observables extracted from cellular SOPs, IMU measurements, and GNSS-derived position estimates (when available). The EKF is coupled with a closed-loop map-matching approach. The framework assumes the positions of the cellular towers to be known and it estimates the vehicle's states (position, velocity, orientation, and IMU biases) along with the difference between the vehicle-mounted receiver clock error states (bias and drift) and each cellular SOP clock error states. Experimental results with cellular long-term evolution (LTE) SOPs are presented, evaluating the efficacy and accuracy of the proposed framework in a deep urban area with a limited sky view. The experimental results demonstrate a position root-mean squared error (RMSE) of 2.8 m over a 1380 m trajectory during which GNSS signals are available and an RMSE of 3.12 m over the same trajectory during which GNSS signals were unavailable for 330 m. Moreover, compared to localization with a traditional GNSS-IMU integrated systems, it is demonstrated that the proposed framework reduces the position RMSE by 22% whenever GNSS signals are available and by 81% whenever GNSS signals are unavailable.**

I. Introduction

Localization technologies for navigation and ground vehicle autonomy levels have been evolving hand in hand. Ten years ago, ground vehicle localization systems for navigation consisted of a GPS receiver, wheel odometer, and an inertial measurement unit (IMU). Localization errors larger than lane-level and periodic dropouts of the navigation solution were tolerable to the driver who had to follow the path drawn on the GPS navigation system. Although localization and some form of path planning from a start location to a desired destination were performed autonomously, the driver had to steer the car, control acceleration, avoid obstacles, change lanes, etc. Today, as ground vehicles evolve by incorporating autonomous-type driving technologies (e.g., cruise control, active steering, collision avoidance, lane detection, etc.) the requirements on localization and navigation technologies become more stringent, necessitating the need of additional sensors (lidar, vision, radar, etc.). Large errors become less tolerable and consistent availability of the navigation solution is critical. For example, it is not enough to estimate on which freeway the vehicle is driving as certain autonomous actions require lane-level localization. This is crucial for intersections, exiting or entering a freeway, or at a junction of different freeways or streets. Moreover, when entering the freeway for instance, the navigation solution must be continuously available to ensure the safety of passengers and other drivers. Looking ahead, as ground vehicles get endowed with full autonomy, robustness and accuracy of their localization and navigation system become of paramount importance. Without a human driver-in-the-loop, one expects not to question the availability of the localization and navigation system and to establish predictable performance of such systems in different driving scenarios.

Despite the promise of global navigation satellite system (GNSS) signals as an accurate sensing modality, in GNSS-challenged environments (e.g., deep urban streets) these signals suffer from different error sources, including signal blockage due to limited sky view and multipath, in addition to nominal GNSS errors, uncertainties in satellite clocks and positions, signal propagation delays in the ionosphere and troposphere, user receiver noise, etc. In such conditions, it is imperative to continuously monitor the integrity of GNSS signals. Integrity monitoring refers to the capability of the system to detect GNSS anomalies and warn the user when the system should not use GNSS measurements [1]. Integrity monitoring frameworks are divided into internal and external categories [2]. External methods leverage a network of ground monitoring stations to monitor the transmitted signals, while internal methods (e.g., receiver autonomous integrity monitoring (RAIM)) typically use the redundant information within the transmitted navigation signals. As shown in [3], the navigation framework can be coupled with these integrity monitoring methods to detect GNSS unreliability and unavailability. In addition to unavailability due to anomalies, GNSS signals may become unavailable in jamming or spoofing situations. It is also often the case that GNSS receivers lose track of the signals in multipath or non-line-of-sight (NLOS) environments, making the GNSS position solution unreliable. In such cases, an integrity monitoring system would alert the user of an unreliable or unavailable position solution. Such integrity monitoring frameworks can be adapted for cellular-based navigation, the details of which can be found in [4].

Traditional vehicular localization and navigation technologies were heavily dependent on GNSS receivers. Over the

This work was supported in part by the Office of Naval Research (ONR) under Grant N00014-16-1-2305 and Grant N00014-16-1-2809 and in part by the National Science Foundation (NSF) under Grant 1751205.

past decade, these systems evolved by coupling GNSS receivers with on-board sensors, such as IMUs. Moreover, such navigation systems may have access to proximity localization techniques (e.g., lidar, camera, and radar), which provide local position information and aid in collision avoidance. Map-matching techniques have also been developed to match the navigation solution obtained by the navigation system to a point in the digital map [3], [5], [6]. More recently, signals of opportunity (SOPs) have been fused with GNSS receivers to complement the GNSS navigation solution [7] or as an alternative to GNSS [8].

This paper considers for the first time the fusion of some of the above readily available off-the-shelf technologies to achieve a highly robust and accurate navigation solution in urban environments by complementing the individual technologies' desirable attributes. Specifically, the developed system uses:

- **GNSS**: GNSS can provide meter-level and submeter-level accurate navigation solution using code and carrier phase measurements, respectively, in a global frame. However, GNSS signals are highly attenuated indoors and in deep urban canyons, which makes them practically unusable in these environments. Moreover, GNSS signals are sensitive to multipath and susceptible to intentional interference (jamming) and counterfeit signals (spoofing), which can wreak havoc in military and civilian applications.
- **IMU**: While IMU sensors provide an accurate short-term navigation solution, one cannot rely on them as a standalone, accurate solution for long-term navigation. This is due to the fact that the noisy outputs of IMUs are integrated through an inertial navigation system (INS), causing pose estimation errors to accumulate over time [9], [10]. The accumulated error rate is dependent on the quality of the IMU. These errors compromise the safe and efficient operation requirements for ground vehicle navigation in urban environments. Thus, for long-term navigation, an IMU sensor becomes unreliable, and an aiding source is needed to correct its drift and improve the navigation solution.
- **Cellular SOPs**: Cellular base transceiver stations (BTSs) are abundant and available in several bands, aggregating to tens of MHz of usable cellular radio frequency spectrum, making them robust against jamming and spoofing attacks or service outage in certain bands or providers. The cellular system BTS configuration, by construction of the hexagonal cells, possesses favorable geometry, which yields low horizontal dilution of precision (HDOP). The received carrier-to-noise ratio from nearby cellular BTSs is commonly tens of dBs higher than that of GNSS space vehicle (SV) signals, making these signals usable for localization purposes in urban environments. However, due to the low elevation angles of cellular towers compared to GNSS SVs, received cellular signals are affected by multipath (e.g., due to buildings, trees, poles, other vehicles, etc.). Nevertheless, cellular signals have a large bandwidth (up to 20 MHz), which is useful to the receiver in detecting and alleviating multipath effects, leading to precise time-of-arrival (TOA) estimates and in turn a precise navigation solution.
- **Map-matching**: Map-matching for ground vehicle navigation has been extensively studied [11]–[14]. It has been shown that a map-matching framework can provide integrity provision at the lane-level [3]. Map-matching can also correct sensor errors [15]–[17]. Moreover, due to the fact that the errors in digital maps are typically smaller than sensor errors, the digital map information can be used to correct the accumulated error in dead-reckoning (DR)-type sensors (e.g., IMUs) [18]. However, digital maps can have displacement errors.

This article presents a robust vehicular localization framework for navigating in both GNSS-available and GNSS-denied urban environments. The article is written in a tutorial fashion with sufficient details about the proposed system and points to references for the interested reader to probe for further details. The proposed framework was tested in different driving scenarios with a comparable performance (within 2-3 meters) of that of an expensive high-end system: one that uses a dual-frequency GNSS with real-time kinematic (RTK) and a tactical-grade IMU. The proposed approach does not rely on GNSS for ground vehicle navigation in urban environments. Instead, it exploits the abundance of ambient cellular SOPs in such environments. It is worth noting that GNSS suffers from other issues beyond lack of coverage such as severe multipath and susceptibility to jamming and spoofing. However, the focus of this paper is to develop a low-cost system that performs well without GNSS, which could be unavailable or unreliable for whatever reason.

The proposed system uses a computationally efficient extended Kalman filter (EKF) to fuse digital map data, IMU data, GNSS-derived position estimate, and cellular SOP pseudoranges. When GNSS signals are unavailable or compromised, the framework extracts navigation observables from cellular signals and fuses them with IMU and map data and continuously estimates the vehicle's states for subsequent time as it navigates without GNSS signals. When GNSS signals are available, the navigation solution is obtained by fusing the IMU data, map data, cellular signals, and GNSS-derived position estimate. In both modes, a closed-loop map-matching approach is developed, where the refined vehicle position estimate obtained from fusing cellular SOP pseudoranges, IMU, GNSS-derived position estimate (if GNSS is available), and digital road maps is used in a feedback to correct estimates of the receiver and cellular SOP clock error states. It is worth noting that the proposed framework does not specifically assume RTK-type GNSS-derived position estimates. Instead, it considers a low-cost GNSS receiver producing a meter-level accurate navigation solution.

Fig. 1 illustrates a high-level diagram of the proposed ground vehicle localization system. Fig. 1(a) illustrates a block diagram of the cellular-aided IMU framework. Fig. 1(b) demonstrates the proposed closed-loop map-matching approach with inputs being GNSS signals, cellular SOP signals, IMU data, and digital road network and the output being the refined navigation solution. In contrast to existing map-

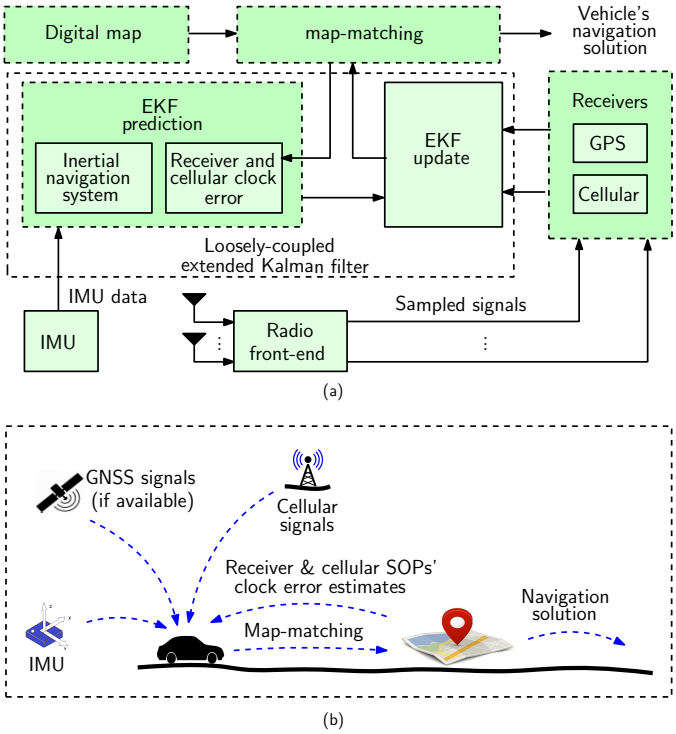

Fig. 1. (a) A high-level diagram of the cellular-aided IMU framework where an IMU sensor is used in a loosely-coupled fashion. (b) The proposed closed-loop map-matching approach. The algorithm is closed-loop where the navigation solution is fed back to correct estimates of the receiver and cellular SOPs clock error states.

matching approaches, the proposed algorithm is closed-loop, where the navigation solution is fed back to correct estimates of the receiver and cellular SOPs clock error states. Note that the problems of localization and navigation are not isolated from each other, but rather closely linked. If a vehicle does not know its exact position at the start of a planned trajectory, it will encounter problems in reaching the destination [19]. Hence, in the sequel, the term navigation is used to capture both localization and navigation purposes.

To evaluate the performance of the proposed ground vehicle navigation algorithm, two experimental tests were performed using ambient cellular long-term evolution (LTE) SOPs in (1) an urban environment where signal attenuation severely affects the received pseudoranges and (2) an environment where SOPs have poor geometric diversity. Experimental results with the proposed method are presented illustrating a close match between the vehicle's true trajectory and the estimated trajectory using the cellular-aided IMU + map data, particularly in a GNSS-denied environment with a limited line-of-sight (LOS) to the open sky. The experimental results demonstrate a position root-mean squared error (RMSE) of 2.8 m over a 1380 m trajectory with available GNSS signals and an RMSE of 3.12 m over the same trajectory during which GNSS signals were unavailable for 330 m. Moreover, it is demonstrated that incorporating the proposed algorithm reduces the position RMSE by 22% and 81%, in GNSS-available and GNSS-denied environments, respectively, from the RMSE obtained by a GNSS-IMU navigation solution.

The remainder of this article is organized as follows. Section II describes the dynamic models for the IMU and SOPs as well as the model for the digital map. Section III proposes an EKF-based framework for fusing IMU, GNSS-derived position estimate, digital map, and cellular pseudoranges in both GNSS-available and GNSS-denied environments. Section IV provides the experimental results and the performance analysis of the proposed framework in deep urban environment with a limited LOS to the open sky. Section V gives concluding remarks.

II. Navigation Framework Model Description

This section describes the models of the different components of the vehicular navigation framework: IMU, cellular SOP, GNSS receiver, and digital map.

A. IMU Measurement Model

An IMU produces measurements of angular rate and specific force. In order to use these measurements, the IMU's orientation, position, velocity, and measurement biases must be estimated. In this work, an IMU state vector $\boldsymbol{x}_v$ consisting of 16 states is used and is given by

$$\boldsymbol{x}_v = \left[{}^{I}_{G}\bar{\boldsymbol{q}}^{\mathsf{T}} \ , \ \boldsymbol{p}_v^{\mathsf{T}} \ , \ \dot{\boldsymbol{p}}_v^{\mathsf{T}} \ , \ \boldsymbol{b}_g^{\mathsf{T}} \ , \ \boldsymbol{b}_a^{\mathsf{T}} \right]^{\mathsf{T}}, \tag{1}$$

where ${}^{I}_{G}\bar{\boldsymbol{q}}$ is a four-dimensional (4-D) unit quaternion representing the IMU's orientation (i.e., rotation from a global frame G to the IMU's body frame I), where frame G is set to be an inertial frame, such as the Earth-centered inertial frame; $\boldsymbol{p}_v \triangleq [p_{v,x}, p_{v,y}, p_{v,z}]^{\mathsf{T}}$ and $\dot{\boldsymbol{p}}_v$ are the three-dimensional (3-D) position and velocity of the vehicle, respectively, expressed in G; and $\boldsymbol{b}_g$ and $\boldsymbol{b}_a$ are the 3-D gyroscope and accelerometer biases, respectively. The IMU's measurements of the angular rate $\boldsymbol{\omega}$ and specific force $\boldsymbol{a}$ are available every T seconds and can be modeled as

$$\boldsymbol{\omega} = {}^{I}\boldsymbol{\omega} + \boldsymbol{b}_g + \boldsymbol{n}_g, \tag{2}$$

$$\mathbf{a} = \mathbf{R}[{}^{I_k}_{G}\bar{\boldsymbol{q}}] \left({}^{G}\mathbf{a}_I - {}^{G}\boldsymbol{g} \right) + \boldsymbol{b}_a + \boldsymbol{n}_a, \tag{3}$$

respectively, where ${}^{I}\boldsymbol{\omega}$ is the IMU's true rotation rate; $\boldsymbol{n}_g$ is a measurement noise vector, which is modeled as a white noise sequence with covariance $\mathbf{Q}_g$; $\mathbf{R}[{}^{I_k}_{G}\bar{\boldsymbol{q}}]$ is the equivalent rotation matrix of ${}^{I_k}_{G}\bar{\boldsymbol{q}}$; ${}^{G}\mathbf{a}_I$ is the IMU's true acceleration in frame G; and $\boldsymbol{n}_a$ is a measurement noise vector, which is modeled as a white noise sequence with covariance $\mathbf{Q}_a$. The evolution of the gyroscope and accelerometer biases are modeled as random walks, i.e., $\dot{\boldsymbol{b}}_a = \boldsymbol{w}_a$ and $\dot{\boldsymbol{b}}_g = \boldsymbol{w}_g$, where $\boldsymbol{w}_a$ and $\boldsymbol{w}_g$ are modeled as zero-mean random vectors with covariances $\sigma^2_{w_a}\mathbf{I}_{3\times 3}$ and $\sigma^2_{w_g}\mathbf{I}_{3\times 3}$, respectively, where $\mathbf{I}_{n\times n}$ denotes an $n\times n$ identity matrix. The equivalent rotation matrix $\mathbf{R}[\bar{\boldsymbol{q}}]$ of the quaternion vector $\bar{\boldsymbol{q}} = [q_0, q_{v_1}, q_{v_2}, q_{v_3}]^{\mathsf{T}}$ is

$$\mathbf{R}[\bar{\boldsymbol{q}}] = [\boldsymbol{r}_1, \boldsymbol{r}_2, \boldsymbol{r}_3], \quad \boldsymbol{r}_1 = \begin{bmatrix} q_0^2 + q_{v_1}^2 - q_{v_2}^2 - q_{v_3}^2 \\ 2(q_{v_1}q_{v_2} - q_0 q_{v_3}) \\ 2(q_{v_1}q_{v_3} + q_0 q_{v_2}) \end{bmatrix},$$

$$\boldsymbol{r}_2 = \begin{bmatrix} 2(q_{v_1}q_{v_2} + q_0 q_{v_3}) \\ q_0^2 - q_{v_1}^2 + q_{v_2}^2 - q_{v_3}^2 \\ 2(q_{v_2}q_{v_3} - q_0 q_{v_1}) \end{bmatrix},$$

$$\boldsymbol{r}_3 = \begin{bmatrix} 2(q_{v_1}q_{v_3} - q_0 q_{v_3}) \\ 2(q_{v_2}q_{v_3} + q_0 q_{v_1}) \\ q_0^2 - q_{v_1}^2 - q_{v_2}^2 + q_{v_3}^2 \end{bmatrix}.$$

The measurements in (2)-(3) will be used in the EKF to perform a time update of the estimate of $\boldsymbol{x}_v$ between measurement updates. This will be discussed in Subsection III-A.

B. GNSS Receiver Measurement Model

The GNSS receiver is assumed to estimate the receiver's 3-D position according to

$$\hat{\boldsymbol{p}}_{\mathrm{GNSS}} = \boldsymbol{p}_{\mathrm{GNSS}} + \boldsymbol{w}_{\mathrm{GNSS}},$$

where $\boldsymbol{p}_{\mathrm{GNSS}} \triangleq [p_{\mathrm{GNSS}_x}, p_{\mathrm{GNSS}_y}, p_{\mathrm{GNSS}_z}]^{\mathsf{T}}$ is the true receiver position, $\boldsymbol{w}_{\mathrm{GNSS}}$ models the uncertainty about this estimate, which is modeled as a zero-mean Gaussian random vector with a covariance $\boldsymbol{\Sigma}_g = \mathrm{diag}\left[{\sigma^2}_{\mathrm{GNSS},x}, {\sigma^2}_{\mathrm{GNSS},y}, {\sigma^2}_{\mathrm{GNSS},z}\right]$. To account for the effect of multipath in urban environment navigation, $\boldsymbol{\Sigma}_{\mathrm{GNSS}}$ consists of nominal errors (e.g., uncertainties in satellite clocks and positions, propagation delays in the ionosphere and troposphere, receiver noise, etc.) as well as multipath, i.e.,

$$\boldsymbol{\Sigma}_g = \boldsymbol{\Sigma}_{\mathrm{GNSS,nom}} + \boldsymbol{\Sigma}_{\mathrm{GNSS,mp}},$$

where $\boldsymbol{\Sigma}_{\mathrm{GNSS,nom}}$ is the covariance of the estimated error due to nominal errors, and $\boldsymbol{\Sigma}_{\mathrm{GNSS,mp}}$ is the covariance of the estimated error due to multipath, which can be obtained from multipath models [20], [21].

C. Cellular SOP Received Signal Model

Cellular towers transmit signals for synchronization and channel estimation purposes. These signals can be used to deduce the pseudorange between the transmitting tower and the receiver. In code division multiple-access (CDMA) systems, a pilot signal consisting of a pseudorandom noise (PRN) sequence, known as the short code, is modulated by a carrier signal and broadcast by each BTS for synchronization purposes [22]. Therefore, by knowing the short code, the receiver may measure the code phase of the pilot signal as well as its carrier phase; hence, forming a pseudorange measurement to each BTS transmitting the pilot signal [23], [24].

Two types of positioning techniques can be defined for LTE, namely network-based and user equipment (UE)-based positioning. In network-based positioning, a positioning reference signal (PRS) is broadcast by the evolved Node B (eNodeB) [25]. The UE uses the PRS to measure the pseudoranges to multiple eNodeBs and transfers the measurements to the network, where the location of the UE is estimated. Over the past few years, research has focused on UE-based positioning techniques, where the broadcast reference signals, namely primary synchronization signal (PSS), secondary synchronization signal (SSS), and cell-specific reference signal (CRS) were explained for navigation purposes [26]. Among these sequences, it was demonstrated that the CRS yields the most precise positioning due to its large transmission bandwidth [27]. CRS is transmitted to estimate the channel between the UE and the eNodeB and could have a bandwidth up to 20 MHz. Several techniques have been proposed to extract the TOA from the CRS such as (1) threshold-based approaches [28], [29], (2) super resolution algorithm [30], and (3) software-defined receivers [31], [32]. Experimental results have shown meter-level positioning accuracy using standalone LTE CRS signals (i.e., without fusing other sensors).

In a very dynamic environment, e.g., for a moving receiver, channel coherence time is relatively small (less than the measurement's sampling time). Therefore, in a line of sight (LOS) condition, the pseudorange error due to the multipath can be modeled with a zero mean white Gaussian sequence and an additive Gaussian noise model is valid for LTE pseudorange measurements. In a NLOS scenario, the receiver tracks the multipath signal instead of the LOS. Therefore, a nonzero bias must be added to the pseudorange measurement model. Research have proposed multiple NLOS identification methods including cooperative and noncooperative techniques [33]. When a NLOS measurement is detected, the receiver can either exclude the measurement from the measurement set or it can reduce its weight to decrease the error due to the NLOS signal [33]. NLOS identification is out of the scope of this research and all measurements are considered to be LOS.

A model of the LOS pseudorange made by the receiver on the n-th cellular SOP is given by [34]

$$\begin{aligned} z_{\mathrm{sop},n}(k) = &\left\|\boldsymbol{p}_v(k) - \boldsymbol{p}_{\mathrm{sop},n}\right\|_2 \\ &+ c \cdot [\delta t_r(k) - \delta t_{\mathrm{sop},n}(k)] + v_{\mathrm{sop},n}(k), \\ &n = 1, \ldots, N_{\mathrm{sop}}, \end{aligned}$$

where N_{sop} is the total number of available cellular SOPs; $\boldsymbol{p}_{\mathrm{sop},n}$ and $\delta t_{\mathrm{sop},n}$ are the 3-D position vector and the clock bias of the n-th cellular SOP transmitter, respectively; and $v_{\mathrm{sop},n}$ is the measurement noise, which is modeled as a zero-mean white Gaussian sequence with variance ${\sigma^2}_{\mathrm{sop},n}$. Note that the pseudorange measurement noise variance includes both the effect of noise and multipath error. Since cellular SOP transmitters are stationary, their positions $\left\{\boldsymbol{p}_{\mathrm{sop},n}\right\}_{n=1}^{N_{\mathrm{sop}}}$ could be readily obtained, e.g., from cellular tower location databases or by mapping them *a priori* [35], [36]. The proposed framework assumes *a priori* knowledge of $\left\{\boldsymbol{p}_{\mathrm{sop},n}\right\}_{n=1}^{N_{\mathrm{sop}}}$. Note that in general, some cellular SOP transmitter positions tend to overlap, due to having base stations from multiple carrier providers on the same physical tower. In this paper, only one cellular SOP is taken from a physical tower location; hence, $\left\{\boldsymbol{p}_{\mathrm{sop},n}\right\}_{n=1}^{N_{\mathrm{sop}}}$ are all different. By virtue of the hexagonal cellular system structure, cellular SOPs from different tower locations tend to be distributed fairly uniformly around the receiver, which significantly reduces the dilution of precision [36]. Optimal performance is obtained when the SOPs form a regular polygon around the receiver when $N_{\mathrm{sop}} \geq 3$ [37]. It was observed from several data sets of LTE signals recorded in vehicular environments that typical values of N_{sop} vary between 3 and 5 for each operator. The 3GPP2 protocol requires cellular base stations to be synchronized to within 10 μs from GPS time [38]. Cellular base stations are typically equipped with GNSS receivers to meet this synchronization

requirement. While this level of synchronization is acceptable for communication purposes, it might introduce significant errors (on the order of tens of meters) in the pseudorange measurements if not accounted for properly, which in turn introduces large errors in the navigation solution. Therefore, each cellular SOP is assumed to have its own clock error states, namely clock bias and drift. Moreover, the SOP clock biases are stochastic and dynamic; hence, they must be continuously estimated. The vehicle-mounted receiver clock error state vector is $\boldsymbol{x}_{\mathrm{clk},r} \triangleq \left[\delta t_r, \dot{\delta} t_r\right]^{\mathsf{T}}$, where $\dot{\delta} t_r$ is the receiver's clock drift, and the n-th cellular SOP clock error state vector is $\boldsymbol{x}_{\mathrm{clk,sop},n} \triangleq \left[\delta t_{\mathrm{sop},n}, \dot{\delta} t_{\mathrm{sop},n}\right]^{\mathsf{T}}$, where $\dot{\delta} t_{\mathrm{sop},n}$ is the transmitter's clock drift [39]. The discrete-time dynamics of $\boldsymbol{x}_{\mathrm{clk},r}$ and $\boldsymbol{x}_{\mathrm{clk,sop},n}$ are given by

$$\boldsymbol{x}_{\mathrm{clk},r}(k+1) = \mathbf{F}_{\mathrm{clk}} \boldsymbol{x}_{\mathrm{clk},r}(k) + \boldsymbol{w}_{\mathrm{clk},r}(k), \tag{4}$$

$$\boldsymbol{x}_{\mathrm{clk,sop},n}(k+1) = \mathbf{F}_{\mathrm{clk}} \boldsymbol{x}_{\mathrm{clk,sop},n}(k) + \boldsymbol{w}_{\mathrm{clk,sop},n}(k), \tag{5}$$

where $\boldsymbol{w}_{\mathrm{clk},r}$ and $\boldsymbol{w}_{\mathrm{clk,sop},n}$ are zero-mean white random sequences with covariances $\mathbf{Q}_{\mathrm{clk},r}$ and $\mathbf{Q}_{\mathrm{clk,sop},n}$, respectively, and

$$\mathbf{F}_{\mathrm{clk}} = \begin{bmatrix} 1 & T \\ 0 & 1 \end{bmatrix},$$

$$\mathbf{Q}_{\mathrm{clk},r} = \begin{bmatrix} S_{\tilde{w}_{\delta t,r}} T + S_{\tilde{w}_{\dot{\delta} t,r}} \frac{T^3}{3} & S_{\tilde{w}_{\dot{\delta} t,r}} \frac{T^2}{2} \\ S_{\tilde{w}_{\dot{\delta} t,r}} \frac{T^2}{2} & S_{\tilde{w}_{\dot{\delta} t,r}} T \end{bmatrix},$$

where T is the sampling time, $S_{\tilde{w}_{\delta t,r}}$ and $S_{\tilde{w}_{\dot{\delta} t,r}}$ are the power spectra of the continuous-time equivalent process noise driving the vehicle-mounted receiver's clock bias and drift, respectively, and $\mathbf{Q}_{\mathrm{clk,sop},n}$ has the same form as $\mathbf{Q}_{\mathrm{clk},r}$ except that $S_{\tilde{w}_{\delta t,r}}$ and $S_{\tilde{w}_{\dot{\delta} t,r}}$ are replaced with the n-th cellular SOP-specific spectra $S_{\tilde{w}_{\delta t,\mathrm{sop},n}}$ and $S_{\tilde{w}_{\dot{\delta} t,\mathrm{sop},n}}$, respectively. The power spectra can be related to the power-law coefficients $\{h_\alpha\}_{\alpha=-2}^{2}$, which have been shown through laboratory experiments to characterize the power spectral density of the fractional frequency deviation $y(t)$ of an oscillator from nominal frequency, namely, $S_y(f) = \sum_{\alpha=-2}^{2} h_\alpha f^\alpha$ [40], [41]. It is common to approximate such relationships by considering only the frequency random-walk coefficient h_{-2} and the white frequency coefficient h_0, which lead to $S_{\tilde{w}_{\delta t,r}} \approx h_{0,r}/2$ $\left(S_{\tilde{w}_{\delta t,\mathrm{sop},n}} \approx h_{0,\mathrm{sop},n}/2\right)$ and $S_{\tilde{w}_{\dot{\delta} t,r}} \approx 2\pi^2 h_{-2,r}$ $\left(S_{\tilde{w}_{\dot{\delta} t,\mathrm{sop},n}} \approx 2\pi^2 h_{-2,\mathrm{sop},n}\right)$ [42], [43].

Since the SOP pseudorange measurement is parameterized by the difference between the receiver's and the SOP's clock biases [39], one only needs to estimate the difference in clock biases and clock drifts. Hence estimating $\boldsymbol{x}_{\mathrm{clk},r}$ and $\boldsymbol{x}_{\mathrm{clk,sop},n}$ individually is unnecessary in this framework; instead, the difference $\Delta\boldsymbol{x}_{\mathrm{clk,sop},n} = c \cdot (\boldsymbol{x}_{\mathrm{clk},r} - \boldsymbol{x}_{\mathrm{clk,sop},n}) \triangleq \left[c\Delta\delta t_{\mathrm{sop},n}, c\Delta\dot{\delta} t_{\mathrm{sop},n}\right]^{\mathsf{T}}$ is estimated, where $c\Delta\delta t_{\mathrm{sop},n} \triangleq c \cdot [\delta t_r - \delta t_{\mathrm{sop},n}]^{\mathsf{T}}$ and $c\Delta\dot{\delta} t_{\mathrm{sop},n} \triangleq c \cdot \left[\dot{\delta} t_r - \dot{\delta} t_{\mathrm{sop},n}\right]^{\mathsf{T}}$. The augmented clock error state is defined as

$$\boldsymbol{x}_{\mathrm{clk,sop}} \triangleq \left[\Delta\boldsymbol{x}_{\mathrm{clk,sop},1}^{\mathsf{T}}, \ldots, \Delta\boldsymbol{x}_{\mathrm{clk,sop},N_{\mathrm{sop}}}^{\mathsf{T}}\right]^{\mathsf{T}}. \tag{6}$$

It can be readily seen that $\boldsymbol{x}_{\mathrm{clk,sop}}$ evolves according to the discrete-time dynamics

$$\boldsymbol{x}_{\mathrm{clk,sop}}(k+1) = \boldsymbol{\Phi}_{\mathrm{clk}} \boldsymbol{x}_{\mathrm{clk,sop}}(k) + \boldsymbol{w}_{\mathrm{clk,sop}}(k), \tag{7}$$

where $\boldsymbol{\Phi}_{\mathrm{clk}} \triangleq \mathrm{diag}\left[\mathbf{F}_{\mathrm{clk}}, \ldots, \mathbf{F}_{\mathrm{clk}}\right]$ and $\boldsymbol{w}_{\mathrm{clk,sop}}$ is a zero-mean white random sequence with covariance $\mathbf{Q}_{\mathrm{clk,sop}}$ given by

$$\mathbf{Q}_{\mathrm{clk,sop}} = c^2 \begin{bmatrix} \mathbf{Q}_{\mathrm{clk,sop},r,1} & \mathbf{Q}_{\mathrm{clk},r} & \cdots & \mathbf{Q}_{\mathrm{clk},r} \\ \mathbf{Q}_{\mathrm{clk},r} & \mathbf{Q}_{\mathrm{clk,sop},r,2} & \cdots & \mathbf{Q}_{\mathrm{clk},r} \\ \vdots & \vdots & \ddots & \vdots \\ \mathbf{Q}_{\mathrm{clk},r} & \mathbf{Q}_{\mathrm{clk},r} & \cdots & \mathbf{Q}_{\mathrm{clk,sop},r,N_{\mathrm{sop}}} \end{bmatrix}.$$

where

$$\mathbf{Q}_{\mathrm{clk,sop},r,i} \triangleq \mathbf{Q}_{\mathrm{clk,sop},i} + \mathbf{Q}_{\mathrm{clk},r}, \qquad \text{for } i = 1, \cdots, N_{\mathrm{sop}}.$$

D. Map Model

Digital maps provide geographical data and location information, which can be used for aligning noisy traces and displaying traversed trajectories. Digital maps are extensively used in modern navigation systems for accurate vehicle guidance and advanced driver-assistance systems (ADAS) functions. To this end, geographical information systems (GISs) are employed to snap the recorded vehicle trajectory trace to the digital road map using map-matching techniques. Map-matching is the process of associating the vehicle's navigation solution with a spatial road map [3], [44]. Map-matching algorithms enhance the navigation solution by incorporating precise road network data and *a priori* information of road features [14]. Map suppliers have dedicated considerable attention recently to develop highly accurate digital maps to meet the requirements of autonomous vehicle navigation in urban environments and intelligent transportation systems [45].

The map used in proposed framework is developed based on an Open Street Map (OSM) database [46] of Riverside, California, U.S.A. OSM is built by a community of mappers that contribute and maintain roads, trails, and railway stations information. A MATLAB-based parser was developed to extract the road coordinates and interpolate map-matched positions between two successive points with a distance greater than a specified threshold. The elevation profile of the road is obtained using Google Earth. Fig. 2 summarizes the steps to extract map-matched points from a digital map. Fig. 2(a) shows the navigation environment in Riverside, California, U.S.A. Fig. 2(b) demonstrates the same area in OSM database, which is downloadable from the OSM website [46]. Fig. 2(c)–(e) show the steps to process the map data and to extract the coordinates of the road. Finally, Fig. 2(f) illustrates the map-matched points before and after interpolation. This area contains 144,670 map-matched points and 185 roads, which are presented in Fig. 2(f) using red circles and blue lines, respectively.

Some approaches in the literature consider the maps to be errorless (e.g., [47], [48]); however, in the proposed approach, a 3-D map displacement error $\boldsymbol{w}_m$ is incorporated to account for inaccuracies in the map, which is modeled as a zero-mean random vector with covariance $\boldsymbol{\Sigma}_m = \mathrm{diag}\left[\sigma^2{}_{m_x}, \sigma^2{}_{m_y}, \sigma^2{}_{m_z}\right]$. To find the map-matched vehicle's position at time-step k, while accounting for the map displacement error, the proposed model finds the closest Mahalanobis

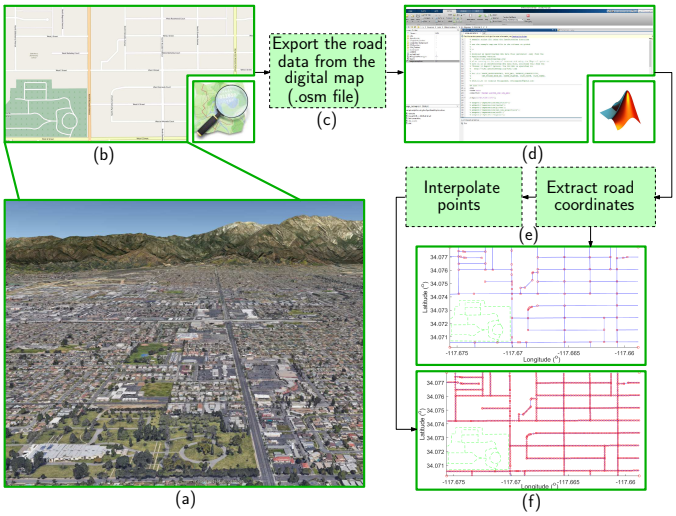

Fig. 2. Steps to extract the map-matched points from a digital map: (a) The navigation environment, (b) OSM digital map, available at: www.openstreetmap.org, (c) exporting the .osm file which contains road data, (d) MATLAB-based parser to extract road data from the .osm file, (e) processing the digital map, including extracting the road coordinates and interpolating points between successive map-matched points with a distance greater than a specified threshold, and (f) the map-matched points before (top) and after (bottom) interpolation.

distance on the map to the estimated vehicle's position at time-step k. The Mahalanobis distance provides a powerful method of measuring how similar some set of observations is to an ideal set of observations with some known mean and covariance. This is discussed in Subsection III-C.

III. Data Fusion and Map-Matching Framework

This section describes an EKF-based framework to fuse IMU measurements with GNSS and cellular pseudoranges to estimate the vehicle's states (1) and clock error states (6). The framework also employs a closed-loop map-matching step to refine the estimates of the clock error states. A vehicle equipped with an IMU described in Subsection II-A is assumed to navigate in an environment comprising N_{sop} cellular SOP transmitters with fully known locations. The framework provides a robust and accurate navigation with and without GNSS signals by exploiting ambient cellular SOPs. In contrast to traditional approaches, which employ an integrated GNSS-IMU systems with a digital map, the proposed framework deals with a unknown dynamic, stochastic error states of cellular SOPs by simultaneously estimating them. These estimates are further refined via a closed-loop map-matching step. The EKF time and measurement update steps are outlined next, followed by the map-matching correction step.

A. EKF Time Update

In this subsection, the EKF time update step is described. The EKF's vector $\boldsymbol{x}$ consists of the vehicle's state $\boldsymbol{x}_v$ (1) and the clock error states (6), i.e.,

$$\boldsymbol{x} = \left[\boldsymbol{x}_v^{\mathsf{T}}, \boldsymbol{x}_{\text{clk,sop}}^{\mathsf{T}}\right]^{\mathsf{T}}.$$

The cellular SOPs are assumed to be stationary with known positions $\{\boldsymbol{p}_{\text{sop},n}\}_{n=1}^{N_{sop}}$. Between measurement updates (whether from GNSS or cellular signals), the IMU's sampled measurements of the angular velocity $\boldsymbol{\omega}$ and linear acceleration $\mathbf{a}$ are used to perform a time update of $\hat{\boldsymbol{x}}(k|j) \triangleq \mathbb{E}\left[\boldsymbol{x}(k)\middle|\{\boldsymbol{z}(i)\}_{i=1}^{j}\right]$, for $k > j$ to get the predicted states $\hat{\boldsymbol{x}}(k+1|j)$ and corresponding prediction error covariance $\mathbf{P}(k+1|j)$. The time update of the orientation state estimate is given by

$$\overset{I_{k+1|j}}{G}\hat{\boldsymbol{q}} = \overset{I_{k+1}}{I_k}\hat{\boldsymbol{q}} \otimes \overset{I_{k|j}}{G}\hat{\boldsymbol{q}}, \tag{8}$$

where $\overset{I_{k+1}}{I_k}\hat{\boldsymbol{q}}$ represents the estimated relative rotation of the IMU from time-step k to $k+1$. In (8), $\otimes$ denotes the quaternion multiplication operator, which operates on two quaternion vectors $\boldsymbol{q}_1 \triangleq [q_{0,1}, q_{v_1,1}, q_{v_2,1}, q_{v_3,1}]$ and $\boldsymbol{q}_2 \triangleq [q_{0,2}, q_{v_1,2}, q_{v_2,2}, q_{v_3,2}]$ to yield

$$\begin{aligned}\boldsymbol{q}_1 \otimes \boldsymbol{q}_2 = [&q_{0,1}q_{0,2} - q_{v_1,1}q_{v_1,2} - q_{v_2,1}q_{v_2,2} - q_{v_3,1}q_{v_3,2},\\ &q_{0,1}q_{v_1,2} + q_{v_1,1}q_{0,2} + q_{v_2,1}q_{v_3,2} - q_{v_3,1}q_{v_2,2},\\ &q_{0,1}q_{v_2,2} - q_{v_1,1}q_{v_3,2} + q_{v_2,1}q_{0,2} + q_{v_3,1}q_{v_1,2},\\ &q_{0,1}q_{v_3,2} + q_{v_1,1}q_{v_2,2} - q_{v_2,1}q_{v_3,2} + q_{v_3,1}q_{0,2}\,]^{\mathsf{T}}.\end{aligned}$$

The value of $\overset{I_{k+1}}{I_k}\hat{\boldsymbol{q}}$ is found by integrating the measurements $\boldsymbol{\omega}(k)$ and $\boldsymbol{\omega}(k+1)$ using a fourth order Runge-Kutta, which yields

$$\begin{aligned}\overset{I_{k+1}}{I_k}\hat{\bar{\boldsymbol{q}}} &= \bar{\boldsymbol{q}}_0 + \frac{T}{2}\left(\boldsymbol{d}_1 + 2\boldsymbol{d}_2 + 2\boldsymbol{d}_3 + \boldsymbol{d}_4\right),\\ \boldsymbol{d}_1 &= \frac{1}{2}\boldsymbol{\Omega}\left(\hat{\boldsymbol{\omega}}(k)\right)\bar{\boldsymbol{q}}_0, \quad \boldsymbol{d}_2 = \frac{1}{2}\boldsymbol{\Omega}\left(\hat{\bar{\boldsymbol{\omega}}}(k)\right)\left(\bar{\boldsymbol{q}}_0 + \frac{1}{2}T\boldsymbol{d}_1\right),\\ \boldsymbol{d}_3 &= \frac{1}{2}\boldsymbol{\Omega}\left(\hat{\bar{\boldsymbol{\omega}}}(k)\right)\left(\bar{\boldsymbol{q}}_0 + \frac{1}{2}T\boldsymbol{d}_2\right),\\ \boldsymbol{d}_4 &= \frac{1}{2}\boldsymbol{\Omega}\left(\hat{\boldsymbol{\omega}}(k+1)\right)\left(\bar{\boldsymbol{q}}_0 + \frac{1}{2}T\boldsymbol{d}_3\right),\\ \hat{\bar{\boldsymbol{\omega}}}(k) &= \frac{1}{2}\left(\hat{\boldsymbol{\omega}}(k) + \hat{\boldsymbol{\omega}}(k+1)\right), \quad \bar{\boldsymbol{q}}_0 = [1,0,0,0]^{\mathsf{T}},\end{aligned}$$

where $\hat{\boldsymbol{\omega}} = \boldsymbol{\omega} - \hat{\boldsymbol{b}}_g$ and

$$\boldsymbol{\Omega}(\boldsymbol{\omega}) = \begin{bmatrix} 0 & \boldsymbol{\omega}^{\mathsf{T}} \\ \boldsymbol{\omega} & \lfloor\boldsymbol{\omega}\times\rfloor \end{bmatrix},$$

$$\lfloor\boldsymbol{\omega}\times\rfloor = \begin{bmatrix} 0 & -\omega_z & \omega_y \\ \omega_z & 0 & -\omega_x \\ -\omega_y & \omega_x & 0 \end{bmatrix}, \quad \boldsymbol{\omega} = [\omega_x, \omega_y, \omega_z]^{\mathsf{T}}.$$

The time update of the velocity estimate is computed using the trapezoidal integration according to

$$\hat{\boldsymbol{p}}_v(k+1|j) = \hat{\boldsymbol{p}}_v(k|j) + \frac{T}{2}\left[\hat{\boldsymbol{s}}(k) + \hat{\boldsymbol{s}}(k+1)\right] + T\,{}^{G}\boldsymbol{g}(k), \tag{9}$$

where $\hat{\boldsymbol{s}}(k) \triangleq \mathbf{R}_{\hat{q}}^{\mathsf{T}}(k)\hat{\boldsymbol{a}}(k)$, $\hat{\boldsymbol{a}}(k) \triangleq \boldsymbol{a}(k) - \hat{\boldsymbol{b}}_a(k|j)$ and $\mathbf{R}_{\hat{q}}(k) \triangleq \mathbf{R}\left[\overset{I_{k|j}}{G}\hat{\boldsymbol{q}}\right]$. The time update of the position estimate is given by

$$\hat{\boldsymbol{p}}_v(k+1|j) = \hat{\boldsymbol{p}}_v(k|j) + \frac{T}{2}\left[\hat{\boldsymbol{p}}_v(k+1|j) + \hat{\boldsymbol{p}}_v(k|j)\right]. \tag{10}$$

The time update of the gyroscope and accelerometer biases estimates is given by

$$\hat{\boldsymbol{b}}_g(k+1|j) = \hat{\boldsymbol{b}}_g(k|j), \quad \hat{\boldsymbol{b}}_a(k+1|j) = \hat{\boldsymbol{b}}_a(k|j). \tag{11}$$

The time update of the clock error state estimate is readily deduced from (7) to be given by

$$\hat{\boldsymbol{x}}_{\mathrm{clk,sop}}(k+1|j) = \boldsymbol{\Phi}_{\mathrm{clk}}\hat{\boldsymbol{x}}_{\mathrm{clk,sop}}(k|j). \tag{12}$$

The time update of the prediction error covariance is given by

$$\mathbf{P}(k+1|j) = \mathbf{F}(k)\mathbf{P}(k|j)\mathbf{F}^{\mathsf{T}}(k) + \mathbf{Q}(k), \tag{13}$$

$$\mathbf{F}(k) \triangleq \mathrm{diag}\left[\boldsymbol{\Phi}_B(k+1,k),\, \boldsymbol{\Phi}_{\mathrm{clk}}\right],$$
$$\mathbf{Q}(k) \triangleq \mathrm{diag}\left[\mathbf{Q}_{d_B}(k),\, \mathbf{Q}_{\mathrm{clk,sop}}\right].$$

The discrete-time INS state transition matrix $\boldsymbol{\Phi}_B$ and process noise covariance $\mathbf{Q}_{d_B}$ are computed using standard INS equations as described in [49], [50].

Remark The four-dimensional quaternion vector is an over-determined representation of the orientation state. To avoid singularities due to this over-determined representation, the estimation error covariance of the three Euler angles is maintained in the EKF. Therefore, the block pertaining to the orientation state in $\mathbf{P}(k|j)$ is 3×3.

B. EKF Measurement Update

When GNSS signals are available, the EKF measurement update stage corrects the time updated states with (i) cellular SOP pseudoranges, (ii) digital map data, and (iii) the estimated vehicle's position obtained from the GNSS navigation solution $\hat{\boldsymbol{p}}_{\mathrm{GNSS}}$.

Here, the measurement vector $\boldsymbol{\mathcal{Z}}(k)$ consists of $\hat{\boldsymbol{p}}_{\mathrm{GNSS}}$ and $\{z_{\mathrm{sop},n}\}_{n=1}^{N_{\mathrm{sop}}}$, where $z_{\mathrm{sop},n}$ is the pseudorange drawn from the n-th cellular SOP transmitter.

When GNSS signals become unavailable, the measurement update stage only uses (i) cellular SOP pseudoranges and (ii) digital map data. Here, $\boldsymbol{\mathcal{Z}}(k)$ only includes cellular SOP measurements, $\{z_{\mathrm{sop},n}\}_{n=1}^{N_{\mathrm{sop}}}$.

Next, the corrected state estimate $\hat{\boldsymbol{x}}(k+1|k+1)$ and associated estimation error covariance $\mathbf{P}(k+1|k+1)$ is computed using the standard EKF measurement update equations [40]. The expressions of the corresponding measurement Jacobian $\mathbf{H}$ and the measurement noise covariance $\boldsymbol{\Sigma}_s$ are demonstrated in Fig. 3.

C. Map-Matching and Closed-Loop Clock Error State Correction

Assuming that the digital map comprises L_N locations, denoted $\left\{\boldsymbol{l}_n \triangleq [p_{m_{x_n}}, p_{m_{y_n}}, p_{m_{z_n}}]^{\mathsf{T}}\right\}_{n=1}^{L_N}$, the position estimate $\hat{\boldsymbol{p}}_v(k|k)$ is map-matched to yield $\hat{\boldsymbol{p}}_m(k|k)$ according to

$$\hat{\boldsymbol{p}}_m(k+1|k+1) = \min_{\boldsymbol{l}_n} \|\hat{\boldsymbol{p}}_v(k+1|k+1) - \boldsymbol{l}_n\|_{\boldsymbol{\Sigma}_m}, \tag{14}$$

where

$$\|\hat{\boldsymbol{p}}_v(k+1|k+1) - \boldsymbol{l}_n\|_{\boldsymbol{\Sigma}_m} = \sqrt{[\hat{\boldsymbol{p}}_v(k+1|k+1) - \boldsymbol{l}_n]^{\mathsf{T}}{\boldsymbol{\Sigma}_m}^{-1}[\hat{\boldsymbol{p}}_v(k+1|k+1) - \boldsymbol{l}_n]}.$$

The estimates $\hat{\boldsymbol{p}}_v(k+1|k+1)$ and $\hat{\boldsymbol{p}}_m(k+1|k+1)$ are fed back to correct the clock bias state estimates according to

$$c\Delta\hat{\delta}t_{\mathrm{sop},n}(k+1|k+1) \longleftarrow c\Delta\hat{\delta}t_{\mathrm{sop},n}(k+1|k+1) + \Delta_{\mathrm{corr},n}(k+1), \tag{15}$$

where

$$\Delta_{\mathrm{corr},n}(k+1) = \|\hat{\boldsymbol{p}}_v(k+1|k+1) - \boldsymbol{p}_{\mathrm{sop},n}\|_2 - \|\hat{\boldsymbol{p}}_m(k+1|k+1) - \boldsymbol{p}_{\mathrm{sop},n}\|_2. \tag{16}$$

Finally, the map-matched estimate $\hat{\boldsymbol{p}}_m(k+1|k+1)$ is used to replace the estimate $\hat{\boldsymbol{p}}_v(k+1|k+1)$, i.e.,

$$\hat{\boldsymbol{p}}_v(k+1|k+1) \longleftarrow \hat{\boldsymbol{p}}_m(k+1|k+1).$$

Fig. 3 summarizes the architecture of the proposed navigation framework.

IV. Experimental Results

To evaluate the performance of the proposed ground vehicle navigation framework, two experimental tests were performed in (1) an urban environment in which GNSS signals get attenuated and become unreliable and (2) an environment in which signals from only 2 cellular LTE towers are used. In both experiments, a ground vehicle was equipped with following hardware and software setup:

- Two consumer-grade 800/1900 MHz cellular omnidirectional Laird antennas [51].
- A Septentrio AsteRx-i V integrated GNSS-IMU, which is equipped with a dual-antenna, multi-frequency GNSS receiver and a Vectornav VN-100 micro-electromechanical system (MEMS) IMU. The AsteRx-i V allows access to the raw measurements from this IMU, which was used for the time update of the orientation, position, and velocity as described in Section III-A. Septentrio's post-processing software development kit (PP-SDK) was used to process carrier phase observables collected by the AsteRx-i V and by a nearby differential GPS base station to obtain a carrier phase-based navigation solution. This integrated GNSS-IMU real-time kinematic (RTK) system [52] was used to produce the ground truth results with which the proposed navigation framework was compared.
- A dual-channel National Instrument (NI) universal software radio peripheral (USRP)-2954R driven by GPS-disciplined oscillator (GPSDO) [53]. This was used to simultaneously down-mix and synchronously sample cellular LTE signals at 10 mega-samples per second (MSPS).
- A laptop computer to store the sampled cellular signals. These samples were then processed by the Multichannel Adaptive TRansceiver Information eXtractor (MATRIX) software-defined radio (SDR) [29], [54], [55], developed by the Autonomous Systems Perception, Intelligence, and Navigation Laboratory at the University of California, Riverside.

In both experiments, the ground vehicle was assumed to have initial access to GNSS signals. This enabled estimating the initial difference between the vehicle-mounted receiver's clock bias and the clock biases of each LTE eNodeB in the

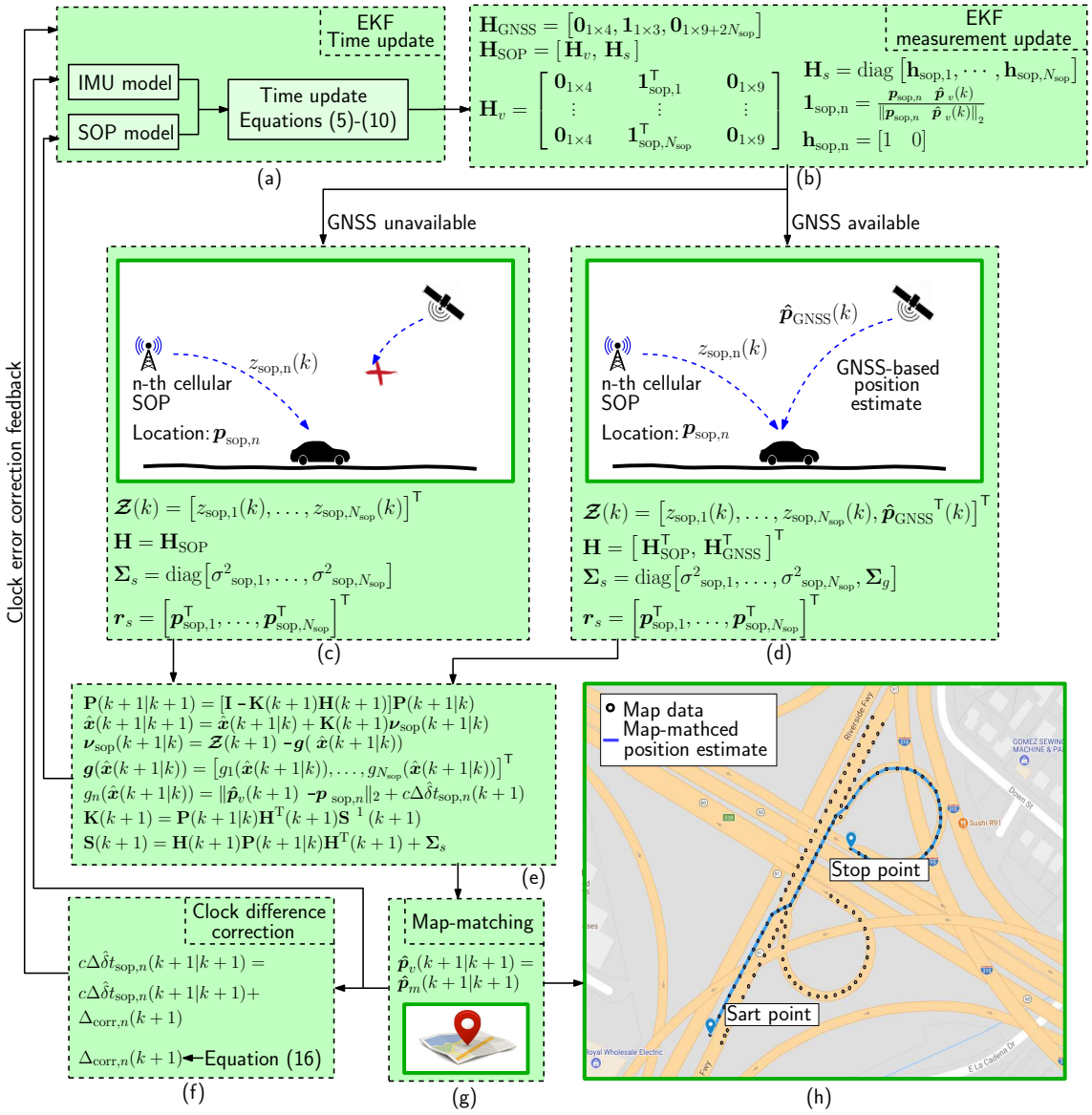

Fig. 3. The architecture of the proposed EKF-based approach in situations where GNSS signals are available and unavailable. (a) EKF time step, (b) EKF measurement update step, (c) measurement update without GNSS signals, (d) measurement update with GNSS signals, (e) corrected state estimate and associated estimation error covariance, (f) calculating the clock difference correction, (g) refining the vehicle's estimated position using the map data, and (h) map-matched vehicle's position estimate.

environment $\{\Delta\hat{\boldsymbol{x}}_{\text{clk,sop},n}(0|-1)\}_{n=1}^{N_{\text{sop}}}$. Moreover, the initial estimates of the vehicle's orientation ${}^{I}_{G}\hat{\bar{\boldsymbol{q}}}_v(0|-1)$, position $\hat{\boldsymbol{p}}_v(0|-1)$, and velocity $\hat{\boldsymbol{p}}_v(0|-1)$ were obtained from the GNSS-IMU system. The gyroscopes' and accelerometers' bias estimates; $\hat{\boldsymbol{b}}_g(0|-1)$ and $\hat{\boldsymbol{b}}_a(0|-1)$, respectively; were initialized by averaging 5 seconds of gravity-compensated IMU measurements at a sampling period of $T = 0.01$ seconds, while the vehicle was *stationary*. The initial uncertainties associated with these state estimates were set to $\mathbf{P}_{{}^{I}_{G}\bar{\boldsymbol{q}}_v}(0|-1) = (1\times10^{-3})\mathbf{I}_{3\times3}$, $\mathbf{P}_{\boldsymbol{p}_v}(0|-1) = \text{blkdiag}\,[3\,\mathbf{I}_{2\times2}, 0]$, $\mathbf{P}_{\dot{\boldsymbol{p}}_v}(0|-1) = \text{blkdiag}\,[0.5\,\mathbf{I}_{2\times2}, 0]$, $\mathbf{P}_{\boldsymbol{b}_g}(0|-1) = \left(3.75\times10^{-9}\right)\mathbf{I}_{3\times3}$, $\mathbf{P}_{\boldsymbol{b}_a}(0|-1) = \left(9.6\times10^{-5}\right)\mathbf{I}_{3\times3}$, and $\mathbf{P}_{\Delta\boldsymbol{x}_{\text{clk,sop},n}}(0|-1) = \text{diag}\,[3, 0.3]$, where $\text{blkdiag}(\cdot)$ and $\text{diag}(\cdot)$ denote a block-diagonal and a diagonal matrix, respectively. The value of $\boldsymbol{\Sigma}_g$ was set to $\text{diag}\,[5, 5, 5]$ m^2 and the SOP measurement noise variances are calculated empirically while the vehicle has access to GNSS signals according to

$$\sigma^2{}_{\text{sop},n} \approx \frac{1}{k_{\text{cutoff}}} \sum_{k=0}^{k_{\text{cutoff}}-1} \hat{v}'^2{}_{\text{sop},n}(k),$$

where k_{cutoff} is the time GNSS signals were cutoff and

$$\hat{v}'_{\text{sop},n}(k) \triangleq z_{\text{sop},n}(k) - \left\|\hat{\boldsymbol{p}}_{\text{GNSS}}(k) - \boldsymbol{p}_{\text{sop},n}\right\|_2 - c\hat{\Delta}\delta t_{\text{sop},n}. \tag{17}$$

Note that (17) assumes that $\hat{v}'_{\text{sop},n}$ is a stationary white sequence. However, in practice, these processes are not necessarily white and therefore a variance inflation factor is needed to account for the colored noise. Hence, $\sigma^2{}_{\text{sop},n} \leftarrow \alpha\sigma^2{}_{\text{sop},n}$, where α is the inflation factor, which was chosen to be two in the experiments presented in this paper.

The following subsections present the navigation results in each of the two environments.

A. Environment 1

The first experiment was conducted in an urban environment: downtown Riverside, California, USA. The vehicle traversed a trajectory of 1380 m in 190 s. The traversed trajectory within this environment was surrounded by tall trees and buildings, which attenuates received cellular and GNSS signals. In fact, due to the low elevation angles of cellular towers compared to GNSS satellites, LOS obstructions (e.g., buildings, trees, poles, other vehicles, etc.) between the tower and the vehicle-mounted receiver are prevalent. Fig. 5 shows the environment and experimental hardware setup. Over the course of the experiment, the receiver was listening to 5 eNodeBs corresponding to the U.S. cellular provider AT&T with the characteristics summarized in Table I. It has been shown that the pseudorange measurement noise variance and multipath error is lower for signals with higher transmission bandwidth [55]. Therefore, LTE signals with a 20 MHz bandwidth can provide more accurate pseudorange measurements compared to LTE signals with a 10 MHz bandwidth. Note that the transmission bandwidth of LTE signals is not unique and depends on the LTE network provider. Fig. 4(a) shows the LTE pseudorange (solid lines) and actual range (dashed lines) variations and Fig. 4(b) shows empirical cumulative distribution function (CDF) of LTE pseudoranges for eNodeBs 1–5. The standard deviations of the pseudoranges for eNodeBs 1–5 were calculated to be 9.19, 3.61, 4.18, 7.75, and 6.01 m, respectively.

TABLE I
LTE ENODEBS CHARACTERISTICS USED IN ENVIRONMENT 1

eNodeB	Carrier frequency (MHz)	Cell ID	Bandwidth (MHz)
1	1955	216	20*
2	739	319	10
3	739	288	10
4	739	151	10
5	739	232	10

* 1024 middle subcarriers used instead of 2048

The performance of the proposed navigation framework is studied in two scenarios.

The first scenario compares the performance against three existing approaches:

(I) GPS-only: this emulates a low-cost technology, which only uses GPS pseudoranges to estimate the vehicle's states.

(II) GPS-IMU: this approach fuses GPS produced positions with an IMU, which exhibits < 10 degrees per hour gyroscope bias stability (such IMU is typically considered a tactical-grade), in a loosely coupled fashion to estimate the vehicle's state.

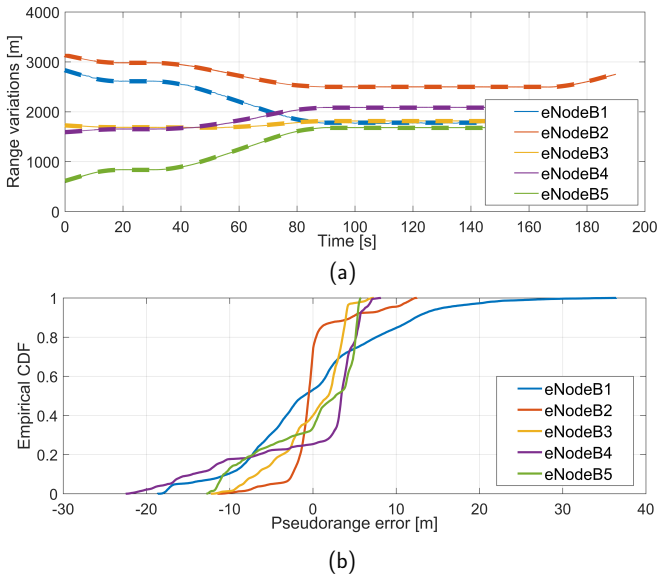

Fig. 4. (a) LTE pseudorange (solid lines) and actual range (dashed lines) variations and (b) empirical cumulative distribution function (CDF) of the LTE pseudoranges for eNodeBs 1–5

(III) GPS-IMU-Map-Matching: this emulates an existing high-end vehicular navigation system, which map-matches the estimated vehicle's position from the GPS-IMU system produced in the second approach above.

The second scenario studies the performance of the proposed framework in the absence of GNSS signals. To this end, the GPS navigation solution $\hat{\boldsymbol{p}}_{\text{GNSS}}$ was discarded in a portion of the vehicle's trajectory to emulate GNSS unavailability (see Fig. 3).

Throughout the experimental test, the PP-SDK was configured to produce a navigation solution at 1 Hz from GPS L1 C/A measurements only to emulate a low-cost, low-quality GPS receiver. In contrast, the ground-truth against which the proposed framework and the three approaches above were compared was produced with the expensive, high-end GNSS-IMU RTK Septentrio AsteRx-i V system.

1) Scenario 1: Comparison Against Existing Technologies: In the first scenario, GPS signals were available along the entire trajectory. Fig. 6 shows the vehicle's ground truth trajectory versus its estimated trajectory from GPS-only, GPS-IMU, and proposed framework. Table II compares the navigation performance of the proposed framework versus that of the three approaches: GPS-only, GPS-IMU, GPS-IMU-Map. It can be seen from these results that the proposed framework outperforms all three approaches. Most notable, the proposed framework, which was a standard GPS receiver whose navigation solution is loosely-coupled with cellular pseudoranges and a closed-loop map-matching, outperforms a high-end vehicular navigation system that uses an expensive tightly-coupled GPS-IMU system with map-matching.

2) Scenario 2: Performance when GNSS Signals are Unavailable: In this scenario, the proposed framework's performance in the absence of GNSS signals was evaluated. To this end, the navigation solution obtained from the GPS receiver was discarded over a portion of 330 m from the total trajectory

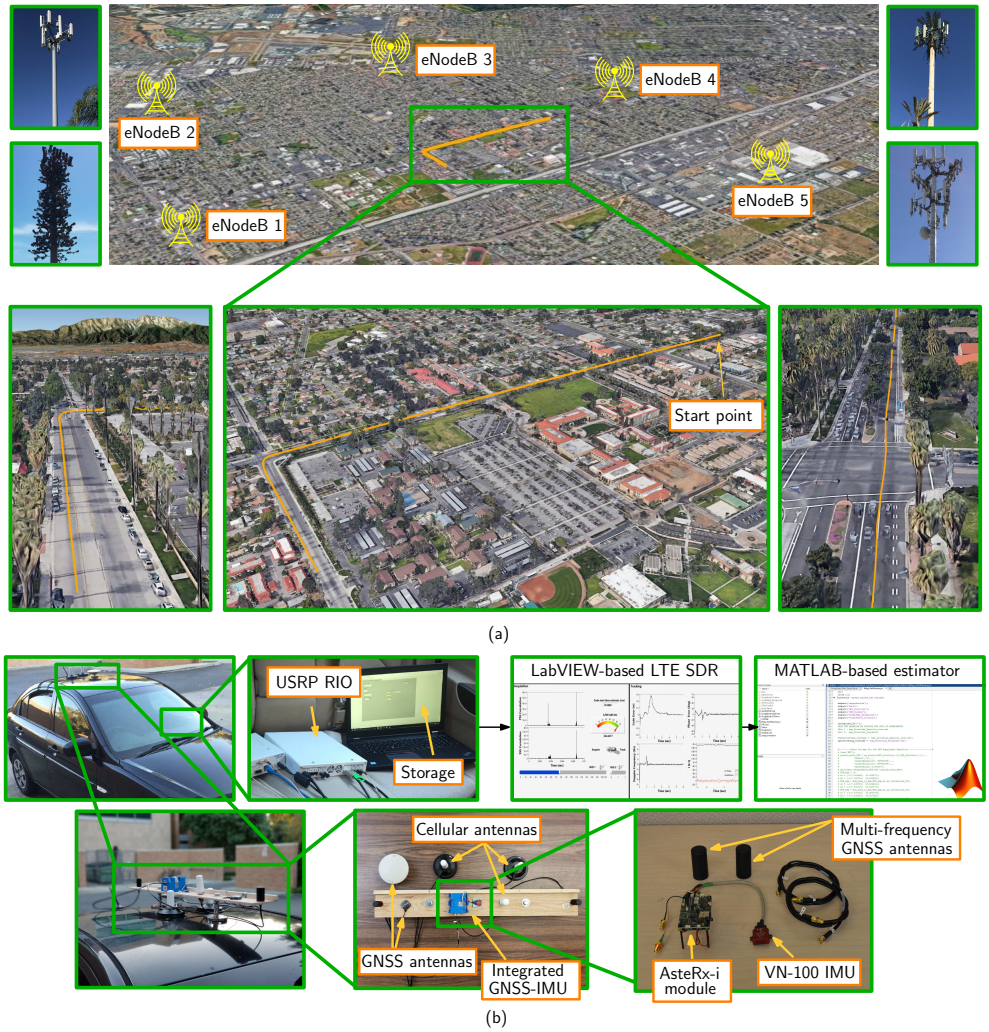

Fig. 5. The experimental environment and the experimental setup. (a) The environment layout, LTE SOP positions, and the true vehicle trajectory. As can be seen, the traversed path was surrounded by the tall trees and the received signal experienced severe attenuation effect. Image: Google Earth. (b) Experimental hardware and software setup. The LTE antennas were connected to a dual-channel NI USRP-2954R driven by a GPSDO. The stored LTE signals were processed via the MATRIX SDR.

TABLE II
NAVIGATION PERFORMANCE COMPARISON IN AN URBAN ENVIRONMENT

Navigation Solution	Position RMSE	Mean distance error	Max. distance error
GPS only	5.61 m	6.18 m	13.30 m
GPS-IMU	4.01 m	4.53 m	10.38 m
GPS-IMU-map	3.03 m	3.54 m	8.40 m
Proposed framework	2.80 m	3.41 m	8.09 m
Improvement over GPS-IMU	30.17%	24.72%	22.06%

to emulate GPS unavailability. Fig. 7 shows the portion of the vehicle's trajectory where GPS signals were unavailable. The vehicle's estimated trajectory from the proposed framework is also shown versus the vehicle's estimated trajectory from the GPS-IMU system. In order to differentiate the influence of the map-matching from the use of LTE measurements, the GPS-IMU-LTE solution (i.e., the proposed framework without map-matching) is also demonstrated in Fig. 7. Table III compares the navigation performance of the proposed framework versus that of the GPS-IMU and GPS-IMU-LTE systems. The following may be concluded from this test scenario. First, as expected, when GPS signals were unavailable, the IMU's solution drifted due to the lack of aiding corrections from GPS signals (red line in Fig. 7). Note that the vehicle came to a stop at the stoplight for 9 seconds, during which the IMU's solution drifted forward and to the right. Subsequently, the IMU's solution continued to drift after the vehicle resumed its forward motion. This error accumulation due to this drift is particularly hazardous for semi-autonomous or fully autonomous ground vehicles. In contrast, the GPS-IMU-LTE solution (green line in Fig. 7) did not exhibit such drift as cellular signals were used as an aiding source to the IMU. Second, the effect of map-matching on the achieved accuracy can be investigated by comparing the GPS-IMU-LTE solution and the proposed solution (yellow line in Fig. 7). As can be

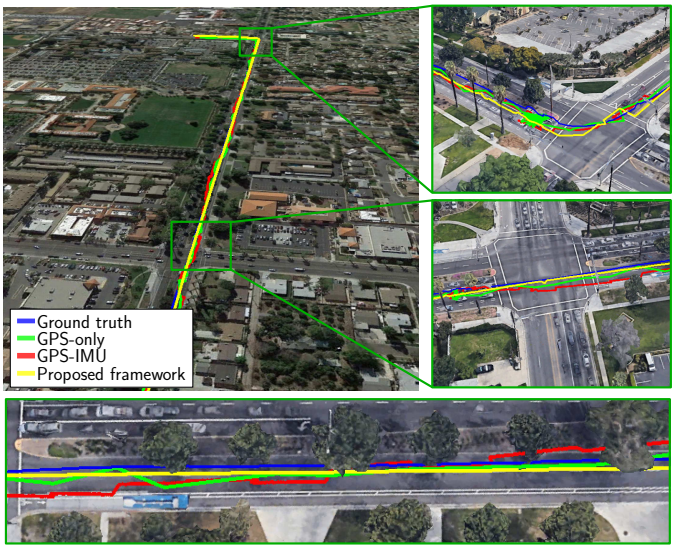

Fig. 6. Experimental results in an urban environment. The vehicle's estimated trajectory with our proposed framework is compared against the estimated trajectory with a GPS-only and a GPS-IMU system. The ground-truth was obtained with an expensive GPS-IMU system with RTK. Experimental results indicate a 2.80 m RMSE for the proposed approach. Image: Google Earth.

seen, the proposed closed-loop framework (i.e., map-matching with clock difference correction) improves the GPS-IMU-LTE solution. The estimated position RMSE using the GPS-IMU-LTE solution was found to be 4.13 m, whereas the estimated position RMSE using the proposed framework was 3.12 m.

TABLE III
NAVIGATION PERFORMANCE COMPARISON WITHOUT GPS SIGNALS

Navigation Solution	Position RMSE	Mean distance error	Max. distance error
GPS-IMU	8.37 m	14.87 m	57.12 m
GPS-IMU-LTE	4.13 m	5.66 m	12.38 m
Proposed framework	3.12 m	4.22 m	10.67 m
Improvement over GPS-IMU	62.72%	71.6%	81.32%

Fig. 7. Vehicle's estimated trajectory from the GPS-IMU system versus our proposed framework when GPS signals become unavailable and then available are specified. As can be seen, the GPS-IMU solution drifts in the absence of GPS signals. In contrast, our proposed framework does not exhibit such drift as cellular signals are used as an aiding source to the IMU. Image: Google Earth.

B. Environment 2

In order to assess the performance of the proposed framework in the case where a small number of cellular towers are available, the second experiment was conducted in a challenging environment in downtown Riverside, California. Here, an urban street with multiple junctions was chosen. The drive test included 15 s of a GNSS cutoff condition. The streets were surrounded by tall buildings from both sides and only 2 LTE towers were available in the environment. Over the course of the experiment, the vehicle-mounted receiver traversed a total trajectory of 345 m while simultaneously listening to 2 LTE SOPs corresponding to the U.S. cellular providers T-Mobile and AT&T. Table IV summarizes the LTE eNodeBs characteristics used in Experiment 2.

TABLE IV
LTE ENODEBS CHARACTERISTICS USED IN ENVIRONMENT 2

LTE SOP	Operator	Carrier frequency (MHz)	Cell ID	Bandwidth (MHz)
1	T-Mobile	2145	79	20
2	AT&T	1955	350	20

Fig. 8 shows the experimental environment, the location of the LTE towers, and the vehicle's ground truth trajectory versus that estimated with the proposed framework and that estimated with the GPS-IMU system. To evaluate the performance of the proposed framework in the absence of GNSS signals, while using signals from only 2 LTE SOPs, the navigation solution obtained from the GPS receiver is discarded over a portion of 40 m of the total trajectory to emulate GPS unavailability. Table V summarizes the navigation performance in this environment. It can be seen that the proposed approach yielded a 32% reduction in the position RMSE and a 43% reduction in the maximum distance error, despite using a very limited number of cellular SOPs.

TABLE V
NAVIGATION PERFORMANCE COMPARISON WITHOUT GPS SIGNALS

Navigation Solution	Position RMSE	Mean distance error	Max. distance error
GPS-IMU	5.10 m	4.75 m	8.96 m
Proposed framework	3.43 m	4.18 m	5.03 m
Improvement over GPS-IMU	32%	18%	43%

V. CONCLUSION

This article presented a novel framework for vehicular navigation in urban environments. The framework uses an IMU, cellular signals, and GNSS signals (when available), along with closed-loop map-matching. On one hand, when GNSS signals are unavailable, the proposed framework uses cellular signals as an aiding source to the IMU, bounding the

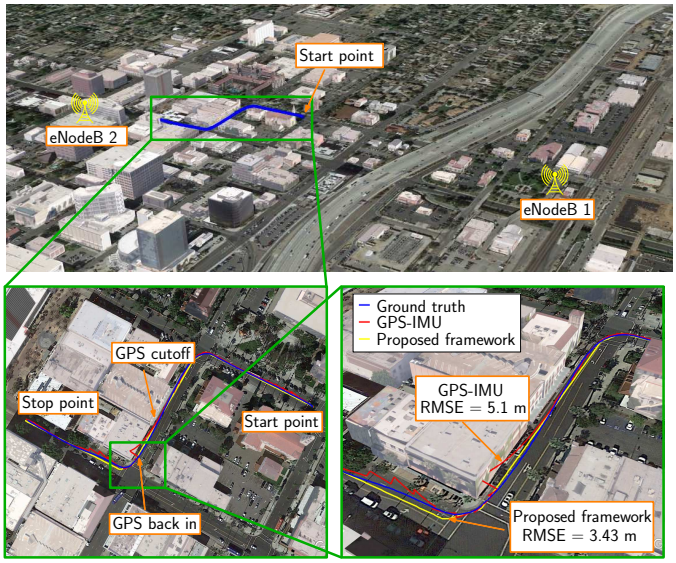

Fig. 8. The second experimental environment layout, LTE SOP positions, true vehicle trajectory, and the different navigation solutions, where the estimated vehicle position obtained from GPS-IMU and the proposed method are shown using yellow and red lines, respectively. Over the course of the experiment, the vehicle-mounted receiver traversed a total trajectory of 345 m in an urban streets while listening to only 2 LTE SOPs simultaneously. It is worth mentioning that in the experiment area, the LTE towers were obstructed by the buildings and the first LTE tower was far from the vehicle, and a large portion of the vehicle's trajectory had no clear LOS to this LTE towers. As can be seen, the estimated position using the proposed framework follows closely the ground truth trajectory during the drive. Experimental results indicate a 3.43 m RMSE for the proposed approach. Image: Google Earth.

IMU drift, and producing an accurate estimate of the vehicle's state. On the other hand, when GNSS signals are available, the proposed framework fuses estimates from the GNSS receiver with cellular measurements to produce an estimate that is within a few meters of the estimate produced by a very expensive, high-end GNSS-IMU system with RTK and map-matching. Experimental results in 2 urban environments are presented demonstrating the accuracy of the proposed framework versus existing technologies. It was demonstrated that the proposed framework achieved a position RMSE of 2.8 m over a trajectory of 1380 m while GNSS signals were available and a position RMSE of 3.12 over the same trajectory while GNSS signals were not available for 330 m. In addition, the robustness of the proposed framework to having a limited number of cellular towers (only 2) was demonstrated, showing a position RMSE of 3.43 m over a trajectory of 345 m, during which GNSS signals were unavailable for 40 m.

REFERENCES

[1] N. Zhu, J. Marais, D. Betaille, and M. Berbineau, "GNSS position integrity in urban environments: A review of literature," *IEEE Transactions on Intelligent Transportation Systems*, vol. PP, no. 99, pp. 1–17, January 2018.

[2] Q. Sun and J. Zhang, "RAIM method for improvement on GNSS reliability and integrity," in *Proceedings of Digital Avionics Systems*, October 2009, pp. 3–11.

[3] R. Toledo-Moreo, D. Betaille, and F. Peyret, "Lane-level integrity provision for navigation and map matching with GNSS, dead reckoning, and enhanced maps," *IEEE Transactions on Intelligent Transportation Systems*, vol. 11, no. 1, pp. 100–112, March 2010.

[4] M. Maaref, J. Khalife, and Z. Kassas, "Integrity monitoring of lte signal of opportunity-based navigation for autonomous ground vehicles," in *Proceedings of ION GNSS Conference*, September 2018, pp. 2456–2466.

[5] M. Rohani, D. Gingras, and D. Gruyer, "A novel approach for improved vehicular positioning using cooperative map matching and dynamic base station dgps concept," *IEEE Transactions on Intelligent Transportation Systems*, vol. 17, no. 1, pp. 230–239, January 2016.

[6] M. Hashemi, "Reusability of the output of map-matching algorithms across space and time through machine learning," *IEEE Transactions on Intelligent Transportation Systems*, vol. 18, no. 11, pp. 3017–3026, November 2017.

[7] J. Morales, J. Khalife, and Z. Kassas, "Opportunity for accuracy," *GPS World Magazine*, vol. 27, no. 3, pp. 22–29, March 2016.

[8] Z. Kassas, J. Morales, K. Shamaei, and J. Khalife, "LTE steers UAV," *GPS World Magazine*, vol. 28, no. 4, pp. 18–25, April 2017.

[9] A. Ramanandan, A. Chen, and J. Farrell, "Inertial navigation aiding by stationary updates," *IEEE Transactions on Intelligent Transportation Systems*, vol. 13, no. 1, pp. 235–248, March 2012.

[10] A. Vu, A. Ramanandan, A. Chen, J. Farrell, and M. Barth, "Real-time computer vision/DGPS-aided inertial navigation system for lane-level vehicle navigation," *IEEE Transactions on Intelligent Transportation Systems*, vol. 13, no. 2, pp. 899–913, June 2012.

[11] Z. He, S. Xi-wei, L. Zhuang, and P. Nie, "Online map-matching framework for floating car data with low sampling rate in urban road networks," *IET Intelligent Transport Systems*, vol. 7, no. 4, pp. 404–414, December 2013.

[12] M. Rohani, D. Gingras, and D. Gruyer, "A novel approach for improved vehicular positioning using cooperative map matching and dynamic base station DGPS concept," *IEEE Transactions on Intelligent Transportation Systems*, vol. 17, no. 1, pp. 230–239, January 2016.

[13] R. Mohamed, H. Aly, and M. Youssef, "Accurate real-time map matching for challenging environments," *IEEE Transactions on Intelligent Transportation Systems*, vol. 18, no. 4, pp. 847–857, April 2017.

[14] G. Jagadeesh and T. Srikanthan, "Online map-matching of noisy and sparse location data with hidden Markov and route choice models," *IEEE Transactions on Intelligent Transportation Systems*, vol. 18, no. 9, pp. 2423–2434, September 2017.

[15] M. Najjar and P. Bonnifait, "A road-matching method for precise vehicle localization using belief theory and Kalman filtering," *Autonomous Robots*, vol. 19, no. 2, pp. 173–191, September 2005.

[16] M. Yu, Z. Li, Y. Chen, and W. Chen, "Improving integrity and reliability of map matching techniques," *Journal of Global Positioning Systems*, vol. 1, no. 10, pp. 40–46, December 2006.

[17] M. Quddus, W. Ochieng, and R. Noland, "Current map-matching algorithms for transport applications: State-of-the art and future research directions," *Transportation Research Part C: Emerging Technologies*, vol. 15, no. 5, pp. 312–328, May 2007.

[18] K. Zhang, S. Liu, Y. Dong, D. Wang, Y. Zhang, and L. Miao, "Vehicle positioning system with multi-hypothesis map matching and robust feedback," *IET Intelligent Transport Systems*, vol. 11, no. 10, pp. 649–658, November 2017.

[19] T. Braunl, *Localization and Navigation*. Springer Berlin Heidelberg, 2008, pp. 241–269.

[20] T. Walter, P. Enge, J. Blanch, and B. Pervan, "Worldwide vertical guidance of aircraft based on modernized GPS and new integrity augmentations," *In Proceedings of the IEEE*, vol. 96, no. 12, pp. 1918–1935, December 2008.

[21] M. Joerger, L. Gratton, B. Pervan, and C. Cohen, "Analysis of Iridium-augmented GPS for floating carrier phase positioning," *NAVIGATION, Journal of the Institute of Navigation*, vol. 57, no. 2, pp. 137–160, 2010.

[22] 3GPP2, "Physical layer standard for cdma2000 spread spectrum systems (C.S0002-E)," 3rd Generation Partnership Project 2 (3GPP2), TS C.S0002-E, June 2011.

[23] J. Khalife, K. Shamaei, and Z. Kassas, "A software-defined receiver architecture for cellular CDMA-based navigation," in *Proceedings of IEEE/ION Position, Location, and Navigation Symposium*, April 2016, pp. 816–826.

[24] J. Khalife, K. Shamaei, and Z. Kassas, "Navigation with cellular CDMA signals – part I: Signal modeling and software-defined receiver design," *IEEE Transactions on Signal Processing*, vol. 66, no. 8, pp. 2191–2203, April 2018.

[25] 3GPP, "Evolved universal terrestrial radio access (E-UTRA); physical channels and modulation," 3rd Generation Partnership Project (3GPP), TS 36.211, January 2011. [Online]. Available: http://www.3gpp.org/ftp/Specs/html-info/36211.htm

[26] K. Shamaei, J. Khalife, and Z. Kassas, "Performance characterization of positioning in LTE systems," in *Proceedings of ION GNSS Conference*, September 2016, pp. 2262–2270.
[27] K. Shamaei, J. Khalife, and Z. Kassas, "Comparative results for positioning with secondary synchronization signal versus cell specific reference signal in LTE systems," in *Proceedings of ION International Technical Meeting Conference*, January 2017, pp. 1256–1268.
[28] F. Knutti, M. Sabathy, M. Driusso, H. Mathis, and C. Marshall, "Positioning using LTE signals," in *Proceedings of Navigation Conference in Europe*, April 2015, pp. 1–8.
[29] K. Shamaei, J. Khalife, and Z. Kassas, "Exploiting LTE signals for navigation: Theory to implementation," *IEEE Transactions on Wireless Communications*, vol. 17, no. 4, pp. 2173–2189, April 2018.
[30] M. Driusso, C. Marshall, M. Sabathy, F. Knutti, H. Mathis, and F. Babich, "Vehicular position tracking using LTE signals," *IEEE Transactions on Vehicular Technology*, vol. 66, no. 4, pp. 3376–3391, April 2017.
[31] J. del Peral-Rosado, J. Lopez-Salcedo, G. Seco-Granados, F. Zanier, P. Crosta, R. Ioannides, and M. Crisci, "Software-defined radio LTE positioning receiver towards future hybrid localization systems," in *Proceedings of International Communication Satellite Systems Conference*, October 2013, pp. 14–17.
[32] K. Shamaei, J. Khalife, S. Bhattacharya, and Z. Kassas, "Computationally efficient receiver design for mitigating multipath for positioning with LTE signals," in *Proceedings of ION GNSS Conference*, September 2017, pp. 3751–3760.
[33] R. Zekavat and R. Buehrer, *Handbook of Position Location: Theory, Practice and Advances*, 1st ed. Wiley-IEEE Press, 2011.
[34] Z. Kassas, "Analysis and synthesis of collaborative opportunistic navigation systems," Ph.D. dissertation, The University of Texas at Austin, USA, 2014.
[35] Z. Kassas, V. Ghadiok, and T. Humphreys, "Adaptive estimation of signals of opportunity," in *Proceedings of ION GNSS Conference*, September 2014, pp. 1679–1689.
[36] J. Morales and Z. Kassas, "Optimal collaborative mapping of terrestrial transmitters: receiver placement and performance characterization," *IEEE Transactions on Aerospace and Electronic Systems*, vol. 54, no. 2, pp. 992–1007, April 2018.
[37] J. Khalife and Z. Kassas, "Navigation with cellular CDMA signals – part II: Performance analysis and experimental results," *IEEE Transactions on Signal Processing*, vol. 66, no. 8, pp. 2204–2218, April 2018.
[38] 3GPP2, "Recommended minimum performance standards for cdma2000 spread spectrum base stations," December 1999.
[39] Z. Kassas and T. Humphreys, "Observability analysis of collaborative opportunistic navigation with pseudorange measurements," *IEEE Transactions on Intelligent Transportation Systems*, vol. 15, no. 1, pp. 260–273, February 2014.
[40] Y. Bar-Shalom, X. Li, and T. Kirubarajan, *Estimation with Applications to Tracking and Navigation*. New York, NY: John Wiley & Sons, 2002.
[41] A. Thompson, J. Moran, and G. Swenson, *Interferometry and Synthesis in Radio Astronomy*, 2nd ed. John Wiley & Sons, 2001.
[42] J. Barnes, A. Chi, R. Andrew, L. Cutler, D. Healey, D. Leeson, T. McGunigal, J. Mullen, W. Smith, R. Sydnor, R. Vessot, and G. Winkler, "Characterization of frequency stability," *IEEE Transactions on Instrumentation and Measurement*, vol. 20, no. 2, pp. 105–120, May 1971.
[43] R. Brown and P. Hwang, *Introduction to Random Signals and Applied Kalman Filtering*, 3rd ed. John Wiley & Sons, 2002.
[44] M. Atia, A. Hilal, C. Stellings, E. Hartwell, J. Toonstra, W. Miners, and O. Basir, "A low-cost lane-determination system using GNSS/IMU fusion and HMM-based multistage map matching," *IEEE Transactions on Intelligent Transportation Systems*, vol. 18, no. 11, pp. 3027–3037, November 2017.
[45] Z. Peng, S. Gao, B. Xiao, S. Guo, and Y. Yang, "CrowdGIS: Updating digital maps via mobile crowdsensing," *IEEE Transactions on Automation Science and Engineering*, vol. PP, no. 99, pp. 1–12, 2017.
[46] Open Street Map foundation (OSMF). [Online]. Available: https://www.openstreetmap.org
[47] P. Bender, J. Ziegler, and C. Stiller, "Lanelets: Efficient map representation for autonomous driving," in *Proceedings of IEEE Intelligent Vehicles Symposium Proceedings*, June 2014, pp. 420–425.
[48] F. Li, P. Bonnifait, J. Ibanez-Guzman, and C. Zinoune, "Lane-level map-matching with integrity on high-definition maps," in *Proceedings of IEEE Intelligent Vehicles Symposium*, June 2017, pp. 1176–1181.
[49] J. Farrell and M. Barth, *The Global Positioning System and Inertial Navigation*. New York: McGraw-Hill, 1998.
[50] P. Groves, *Principles of GNSS, Inertial, and Multisensor Integrated Navigation Systems*, 2nd ed. Artech House, 2013.
[51] Laird phantom 3G/4G multiband antenna NMO mount white TRA6927M3NB. [Online]. Available: https://www.lairdtech.com/products/phantom-series-antennas
[52] (2018) Septentrio AsteRx-i V. [Online]. Available: https://www.septentrio.com/products
[53] National instrument universal software radio peripheral-2954r. [Online]. Available: http://www.ni.com/en-us/support/model.usrp-2954.html
[54] Z. Kassas, J. Khalife, K. Shamaei, and J. Morales, "I hear, therefore I know where I am: Compensating for GNSS limitations with cellular signals," *IEEE Signal Processing Magazine*, pp. 111–124, September 2017.
[55] K. Shamaei and Z. Kassas, "LTE receiver design and multipath analysis for navigation in urban environments," *NAVIGATION, Journal of the Institute of Navigation*, vol. 65, no. 4, pp. 655–675, December 2018.

Zaher (Zak) M. Kassas (S'98-M'08-SM'11) is an assistant professor at the University of California, Riverside (UCR) and director of the Autonomous Systems Perception, Intelligence, and Navigation (ASPIN) Laboratory. He received a B.E. in Electrical Engineering from the Lebanese American University, an M.S. in Electrical and Computer Engineering from The Ohio State University, and an M.S.E. in Aerospace Engineering and a Ph.D. in Electrical and Computer Engineering from The University of Texas at Austin. In 2018, he received the NSF Faculty Early Career Development Program (CAREER) award. His research interests include cyber-physical systems, estimation theory, navigation systems, autonomous vehicles, and intelligent transportation systems.

Mahdi Maaref is a postdoctoral research fellow at UCR. He received the B.E degree in Electrical Engineering from the University of Tehran in 2008 and M.Sc. degree in Electrical Engineering-Power System at the same University in 2011 and Ph.D. Degree in Electrical Engineering at Shahid Beheshti University, Tehran, Iran in 2016. He was a visiting research collaborator at the University of Alberta, Edmonton, Canada in 2016. His main interest is on opportunistic perception, distributed estimation and real-time systems.

Joshua J. Morales (S'11) is a Ph.D. candidate at UCR and a member of the ASPIN Laboratory. He received a B.S. in ECE with High Honors from UCR. His research interests include estimation, navigation, autonomous vehicles, and intelligent transportation systems.

Joe J. Khalife (S'15) is a Ph.D. candidate at UCR and a member of the ASPIN Laboratory. He received a B.E. in EE and an M.S. in Computer Engineering from LAU. His research interests include opportunistic navigation, autonomous vehicles, and SDR.

Kimia Shamaei (S'15) is a Ph.D. candidate at UCR and a member of the ASPIN Laboratory. She received a B.S. and an M.S. in EE from the University of Tehran. Her current research interests include analysis and modeling of signals of opportunity and SDR.